J Mater Sci (2023) 58:1229–1242

Materials for life sciences

Effect of Zn content on 3D gel-printed porous Mg–Zn scaffolds for bone engineering

Tao Lin[1,*], Jianhui Dong[1], Xueting Wang[1], Xin Deng[2,3,*], and Huiping Shao[1]

[1] Institute for Advanced Materials and Technology, University of Science and Technology Beijing, Beijing 100083, People's Republic of China

[2] School of Electromechanical Engineering, Guangdong University of Technology, Guangzhou 510006, People's Republic of China

[3] Jihua Laboratory, Chengye Mansion, 13 Nanpingxi Road, Guicheng Nanhai, Foshan 528299, Guangdong, People's Republic of China

Received: 11 September 2022
Accepted: 19 December 2022
Published online: 5 January 2023

ABSTRACT

This study successfully prepared porous magnesium–zinc (Mg–*x*Zn, *x*: mass ratio of Zn) scaffolds by the 3D gel-printing method. The effect of adding a large percentage of Zn content on porous Mg–*x*Zn scaffolds was also investigated to comprehensively evaluate the effect of Zn on magnesium alloys. The viscosity of slurry decreases with the increase in Zn content. The optimum solid content of slurry suitable for printing is about 60%. The compressive strength of pure Mg, 0.9Mg–0.1Zn, 0.7Mg–0.3Zn, and 0.5Mg–0.5Zn porous scaffolds were 6.29 MPa, 13.03 MPa, 7.69 MPa, and 6.61 MPa, respectively, meeting the requirements of cancellous bone (0.1–16 MPa). In vitro degradation results showed that the degradation rate of Mg scaffolds can be slowed down by adding the appropriate amount of Zn. The fine and dispersed second-phase precipitation can improve the comprehensive properties of Mg–Zn alloy. This study facilitates a comprehensive evaluation of the effect of Zn content on 3D gel-printed magnesium scaffolds.

Introduction

Due to severe trauma, tumor resection, congenital malformation, and other reasons, we need to fill the bone tissue with transplanted bone tissue or substitutes to help it grow [1]. In recent years, Mg scaffolds research has received widespread attention. Magnesium has the advantages of similar density to the human body, lightweight, good strength, and good biocompatibility. The main advantage of magnesium over other biometallic materials is its degradability [2]. The magnesium ions released by degradation can stimulate bone formation, and porous magnesium scaffolds with interconnected pores

Handling Editor: Annela M. Seddon.

Address correspondence to E-mail: lintao@ustb.edu.cn; ruddy.david@qq.com

https://doi.org/10.1007/s10853-022-08108-5

are more conducive to the growth of bone tissue [3, 4]. Degradation products can also be gradually excreted through metabolism, eliminating the pain caused by the second operation and saving medical costs [5].

However, the chemical nature of Mg is very active, especially in the environment of Cl^-, which is highly corrosive and degradable [6]. To improve the mechanical properties and corrosion resistance of magnesium, alloying, improved processing, or surface modification are usually used to enhance the properties [7–10]. Alloying additives include Al, Zn, Zr, and some rare earth elements [11–14]. Studies have shown that adding the above alloying elements obviously improves the corrosion of Mg alloys. However, Al^{3+} easily induces Alzheimer's disease, Zr element increases cancer risk, and rare earth elements have specific toxicity [15]. As an essential element of the human body, Zn has good biocompatibility to promote the growth of bone cells [16]. Therefore, Mg–Zn alloy was selected as the object of this study.

There are many methods to prepare magnesium alloy scaffolds, such as powder metallurgy, particle infiltration, and melt casting. However, these more traditional manufacturing techniques cannot achieve more complex networked 3D architectures with internal interconnections [17]. The recent rapid development of 3D printing [18–20] makes it possible to achieve near-net shapes through 3D modeling for "private customization." Laser-based additive manufacturing techniques prepare magnesium scaffolds with high accuracy, but the high flammability of magnesium powder with a high affinity for oxygen poses a challenge [21–23]. In contrast, a novel 3D gel-printing (3DGP) method offers advantages such as increased safety, less susceptibility to oxidation, short production cycle time, low production cost, and the ability to achieve near-net shapes. In our previous study, 3DGP was developed and has been used to prepare several kinds of material, such as metals [18] and ceramics [19, 20]. Therefore, this printing method has certain acceptability.

To the best of our knowledge, due to the properties of magnesium powder, the selection of suitable adhesive components for magnesium powder is limited, so there are few reports on magnesium powder 3DGP printing methods. In this study, Mg–xZn, (x = 10%, 30%, 50%) scaffolds were successfully printed by our self-developed gel formulation of the epoxy resin system, and the scaffolds were flat in appearance. The mechanical properties met the implantation requirements.

Furthermore, it was found that studies on Mg–Zn alloys still focus on a small percentage of Zn content (1–7 wt%), and the variation of their properties is closely related to intermetallic compounds. Cai et al. [24] have already studied magnesium alloys with 1, 5, 7 wt% Zn addition and showed that adding more than 5 wt% Zn content reduces the corrosion resistance of magnesium alloys. There are no reports on larger percentages of Zn. This paper discusses the effects of 10, 30, and 50 wt% Zn on Mg–Zn alloy, and the role of elemental Zn on the mechanical and degradation properties of Mg alloys is comprehensively evaluated in conjunction with previous studies on smaller percentages of Zn.

Materials and methods

Materials preparation

Mg powder (99.8%, Tangshan Weihao Magnesium Powder Co., Ltd.) and Zn powder (99.8%, Beijing Xingrongyuan Technology Co., Ltd.) were homogeneously mixed by a ball-milling for 2 h to obtain Mg–xZn mixed powders (x = 0, 10, 30, 50 wt%). Deionized water, absolute ethanol, epoxy resin, and oleic acid (AR, Sinopharm Chemical Reagent Co., Ltd.) were used in this study.

Printing process of porous Mg–xZn scaffolds

The epoxy resin was added to the absolute ethanol and stirred to dissolve to form a premixed solution. Then Mg–xZn mixed powder and oleic acid were added, while stirring until the slurry was smooth and uniform. The prepared slurry is loaded into the printer, and the printer was able to print autonomously according to the previously imported 3D scaffolds model. Figure 1 is a schematic diagram of porous Mg–xZn scaffolds prepared by the 3DGP. In our previous research, we successfully printed ceramics [20], cemented carbide [25], and stainless steel [26] with the technology. Finally, the samples are printed.

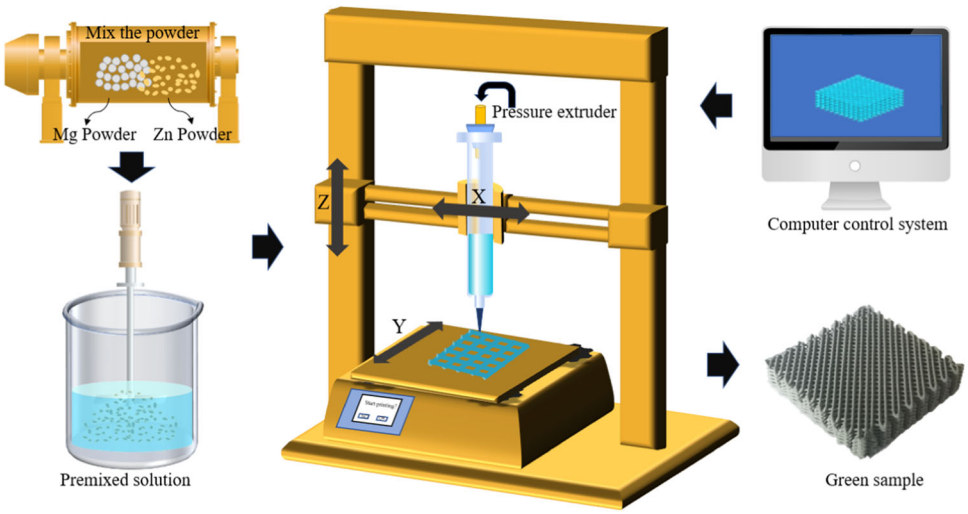

Figure 1 Three-dimensional schematic diagram of porous Mg–xZn scaffolds prepared by the 3DGP process.

Characterization of porous Mg–xZn scaffolds

The particle size distribution of Mg–xZn powders was tested by a laser particle analyzer (BT-9300S, China Dandong Baxter Co., Ltd.) using ethanol as medium. The viscosity of the slurry was tested by an HBDV-1 digital viscometer with 0.3–90 rpm. The shear rate is derived according to the formula of Krieger Dougherty:

$$\mu_r = \left(1 - \frac{\Phi}{\Phi_m}\right)^{-[\mu]\Phi_m}$$

Φ is the volume fraction of the slurry system, Φ_m is the maximum volume fraction of the slurry system, and $[\mu]$ is intrinsic viscosity, usually 2.5 for a sphere. The product of $[\mu]$ and Φ_m is between 1 and 2, generally.

The microstructure of the samples was characterized by scanning electron microscopy (SEM, ZEISS EVO 18, Carl Zeiss NTS, Germany), and the porosity of the sintered samples was determined in absolute ethanol by the Archimedes drainage method. The compressive strength of the samples was tested by a universal electronic tester (CMT5504, SUST Zhuhai) at a loading rate of 0.1 mm/min. The samples used for compressive strength were about 8 mm × 8 mm × 4 mm, then finally grounded with 2000 mesh sandpaper. Data points were collected from three samples for density and compression tests. EM-1500L micro-Vickers hardness tester was used to test the scaffolds for 10 s under 10 gF load and took the average value of five test groups.

In vitro degradation of porous Mg–xZn scaffolds

In advance, 1000 ml of simulated body fluid (SBF) with a pH of 7.4 was prepared. The sintered and polished scaffolds were immersed in SBF solution based on the ratio of scaffold volume to SBF volume of 0.1:6. The pH of the solution was measured every five minutes. The immersion process was carried out in a constant temperature 36 °C water bath. According to the test method proposed by Yin et al. [27], the hydrogen analysis experiments were carried out. The volume of hydrogen released at the time gradient was recorded during the 2 h immersion, and the degradation rate was assessed based on the amount of hydrogen precipitated. After soaking for one hour, Mg, 0.7Mg–0.3Zn, and 0.5Mg–0.5Zn scaffolds collapsed, while 0.9Mg–0.1Zn scaffolds remained intact. Therefore, the weight loss rate of 0.9Mg–0.1Zn scaffolds was tested, and their macro-degradation state was recorded.

The electrochemical corrosion test was performed by a CS350H electrochemical workstation, a three-electrode system consisting of a cleaned sample wafer as a working electrode, a platinum wire as an auxiliary electrode, and a saturated calomel electrode (SCE) as a reference electrode. Potentiodynamic polarization curves were obtained at a scanning rate of 0.5 mV/s in a potential range of $E_{ocp} \pm 250$ mV.

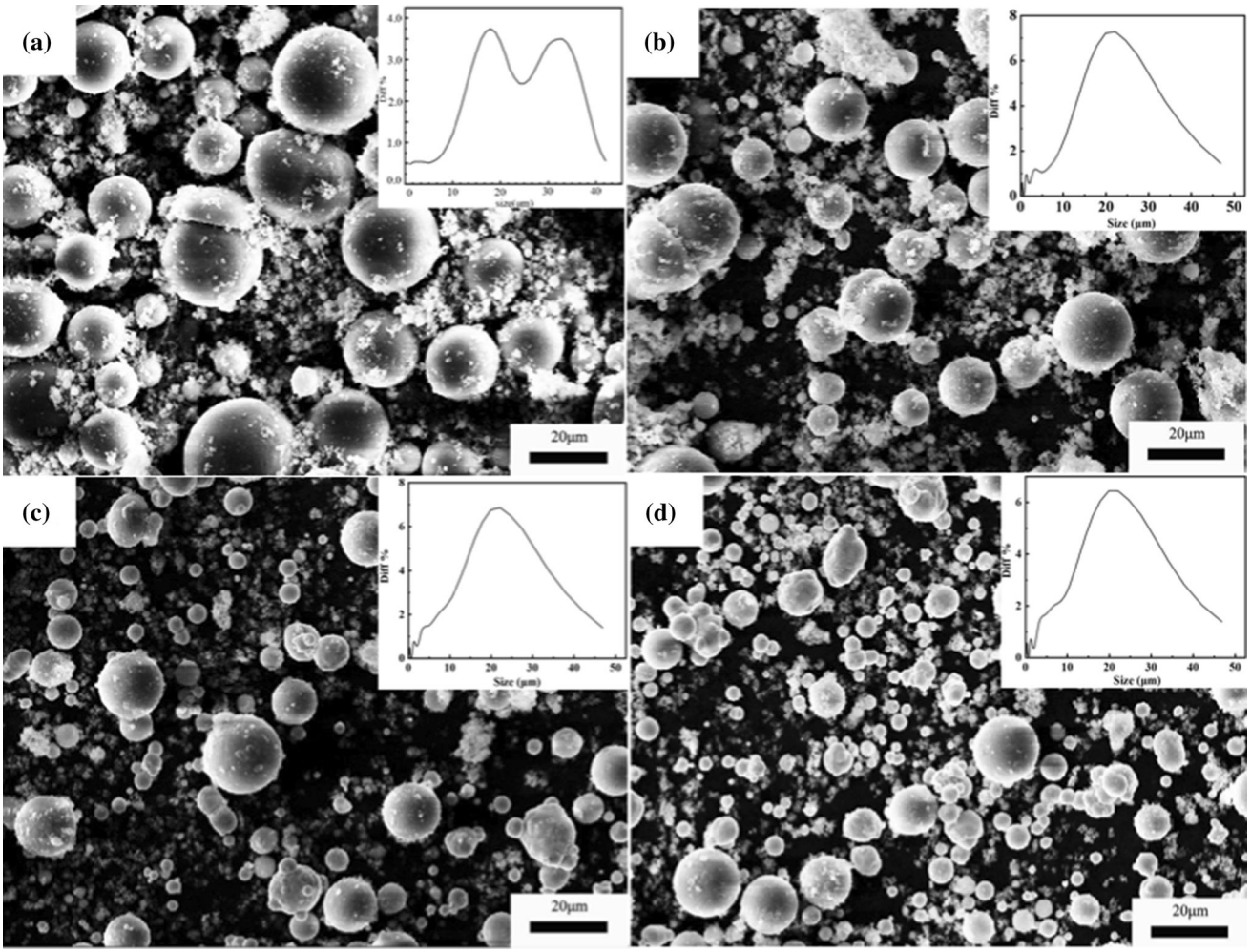

Figure 2 SEM images and particle size distribution of material Mg–Zn powder for 3DGP: **a** Mg, **b** 0.9Mg–0.1Zn, **c** 0.7Mg–0.3Zn, **d** 0.5Mg–0.5Zn.

Biocompatibility evaluation of Mg–Zn scaffolds

Biocompatibility of the 0.9Mg–0.1Zn scaffold was assessed by in vitro culture of mouse-derived osteoblasts MC3T3-E1 (Cell Resource Center of Shanghai Institute for Biological Science, Shanghai, China) with live/dead staining. MC3T3-E1 osteoblasts were cultured in a 5% CO_2 incubator at 37 °C until the cell fusion rate reached approximately 70%. The scaffolds were sterilized under autoclaving. According to ISO 1099312 and GB/T 16886.12–2017 standards, culture medium (DMEM, Corning) containing 10% fetal bovine serum was extracted after holding at 37 °C for 72 h. The extracts were prepared at a concentration of 0.2 g/ml. The medium was replaced with the extracts, and the medium was changed every 3 days. Fluorescent staining of the scaffolds was performed at 1, 3, and 7 days to observe the survival of MC3T3-E1 cells.

Statistical analysis

All quantitative data were expressed as mean standard deviation (SD) (n = 3 for each group of compression test, n = 5 per hardness test, and n = 3 per immersion and cell test per analysis). The results were analyzed via one-way analysis of variance (ANOVA), and $^{\#}P$ value < 0.05 was considered statistically significant.

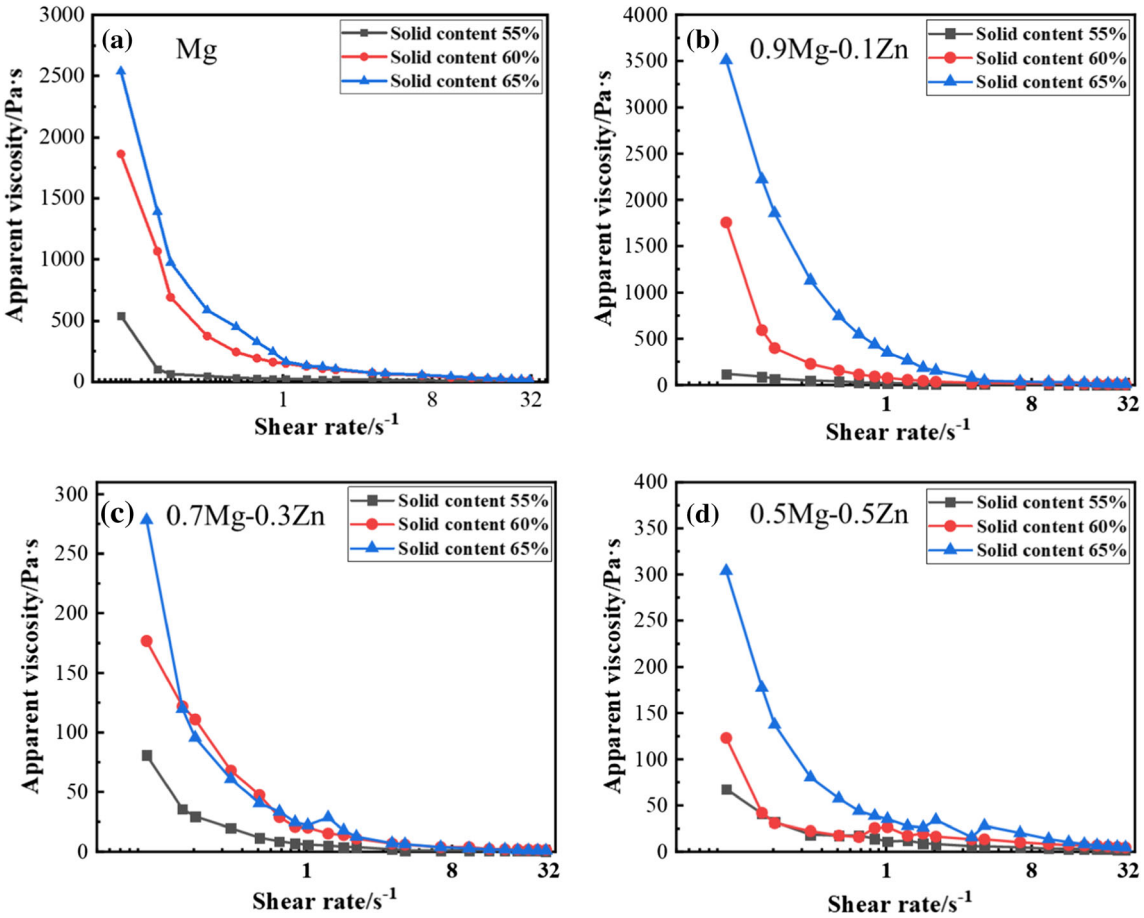

Figure 3 Apparent viscosity of Mg–*x*Zn printing slurry.

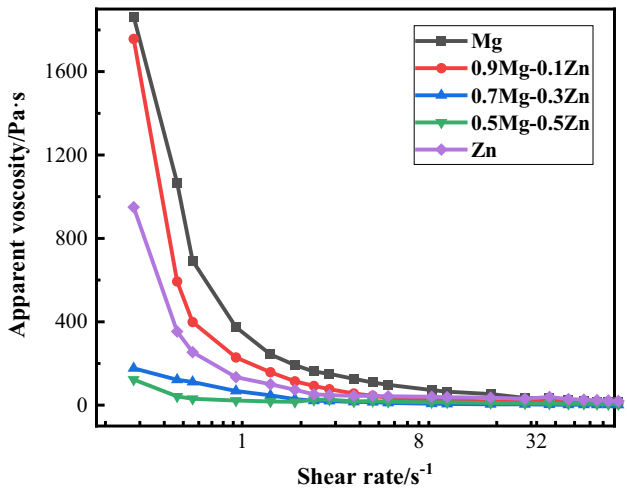

Figure 4 Relative curves between apparent viscosity and shear rate for Mg–*x*Zn printing slurry with 60% solid content.

Results and discussion

Rheological properties of Mg–*x*Zn 3D printing slurry

Slurry properties are essential for the successful preparation of Mg–*x*Zn scaffolds. The SEM images and particle size distribution of Mg powder and Zn powder for 3DGP are shown in Fig. 2. Mg and Zn powders were produced by aerosolization, so the powder shape is spherical, which facilitates 3D printing. When the content of Zn is 0, 10 wt%, 30 wt%, and 50 wt%, the particle sizes of the powder are 18.86 ± 1.101 μm, 17.39 ± 1.829 μm, 16.54 ± 1.879 μm, and 16.39 ± 1.972 μm, respectively. Since the particle size of Zn powder is smaller than that of magnesium powder, the overall particle size of the mixed powder decreases as the Zn content increases. The smaller the particle size, the better the smooth extrusion of 3DGP slurry, and the better the quality of printed sample.

Table 1 Printing parameters of 3DGP for porous Mg–*x*Zn scaffolds

Printing parameters	Nozzle diameter (mm)	Layer height (mm)	Printing speed (mm/s)	Pressure (MPa)
Value	0.51	0.4	6	0.6

The key to successful 3DGP printing of high-quality samples is the preparation of the slurry. Different powder materials and different composition ratios have different slurry parameters. Figure 3 shows the viscosity curves of Mg–*x*Zn printing slurries with different Zn contents. The analysis found that the viscosity of the slurry gradually decreases with the increasing shear rate. This conclusion is consistent with the research results of Dong et al. [17]. The slurry can be extruded smoothly during the printing process because of thinning shear. After extruding, the shear force disappears, and the viscosity increases. For a slurry with the same magnesium content, both the maximum solid content Φ_{max} and the characteristic viscosity [μ] are constants. According to the Krieger Dougherty formula, the apparent viscosity of the slurry increases as the solid content increases. When the solid content is 55%, the viscosity of the slurry is low, and the scaffolds does not form during printing. The slurry will block the printing holes. When the solid content is 65%, the viscosity of the slurry is high, and the printing speed is slow during printing. The printing filament cannot be squeezed out or blocked by the needle. Therefore, after the measurement of Mg and three Mg–Zn mixed powder slurries, 60% solid content is most suitable for preparing Mg alloy scaffolds for printing.

Figure 4 shows the relative curve between apparent viscosity and shear rate for Mg–*x*Zn printing slurries with a solid content of 60%. When the shear rate is 0.5 s^{-1}, the viscosity of Mg, 0.9Mg–0.1Zn, 0.7Mg–0.3Zn, and 0.5Mg–0.5Zn is 1066.19 Pa s, 593.40 Pa s, 121.92 Pa s and 42.11 Pa s, respectively. The cross-sectional comparison analysis shows that with the increase in Zn content, the apparent viscosity decreases, and the lower viscosity is more conducive to the smooth extrusion of the slurry. The reason may be that different powder raw materials have different viscosity ranges. Pure Mg powder raw material slurry viscosity value is large. (When the shear rate is 0.279 s^{-1}, the viscosity is 1863.136 ± 1.5 Pa s.) By comparison, the slurry viscosity value of pure Zn is small. (When the shear rate is 0.279 s^{-1}, the viscosity is 949.727 ± 1.2 Pa s.) Therefore, adding more raw materials with less viscosity of Zn powder will make the overall viscosity value of the mix decrease. The viscosity of the slurry reduces with decreasing powder size for the same solid content and shear rate. The slurry is easier to extrude.

According to the formula of Krieger Dougherty, under the same solid content, the powder size distribution is wide, the tiny particles are embedded in large particles, and Φ_m increases. For the slurry system in this paper, Φ is 60%. Φ_m increases with the

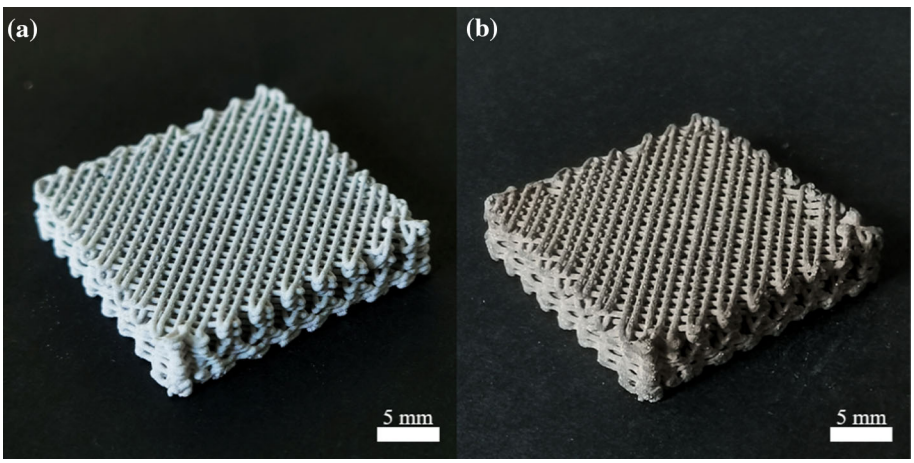

Figure 5 Photographs of porous Mg scaffolds printed by 3DGP: **a** green sample; **b** sintered sample.

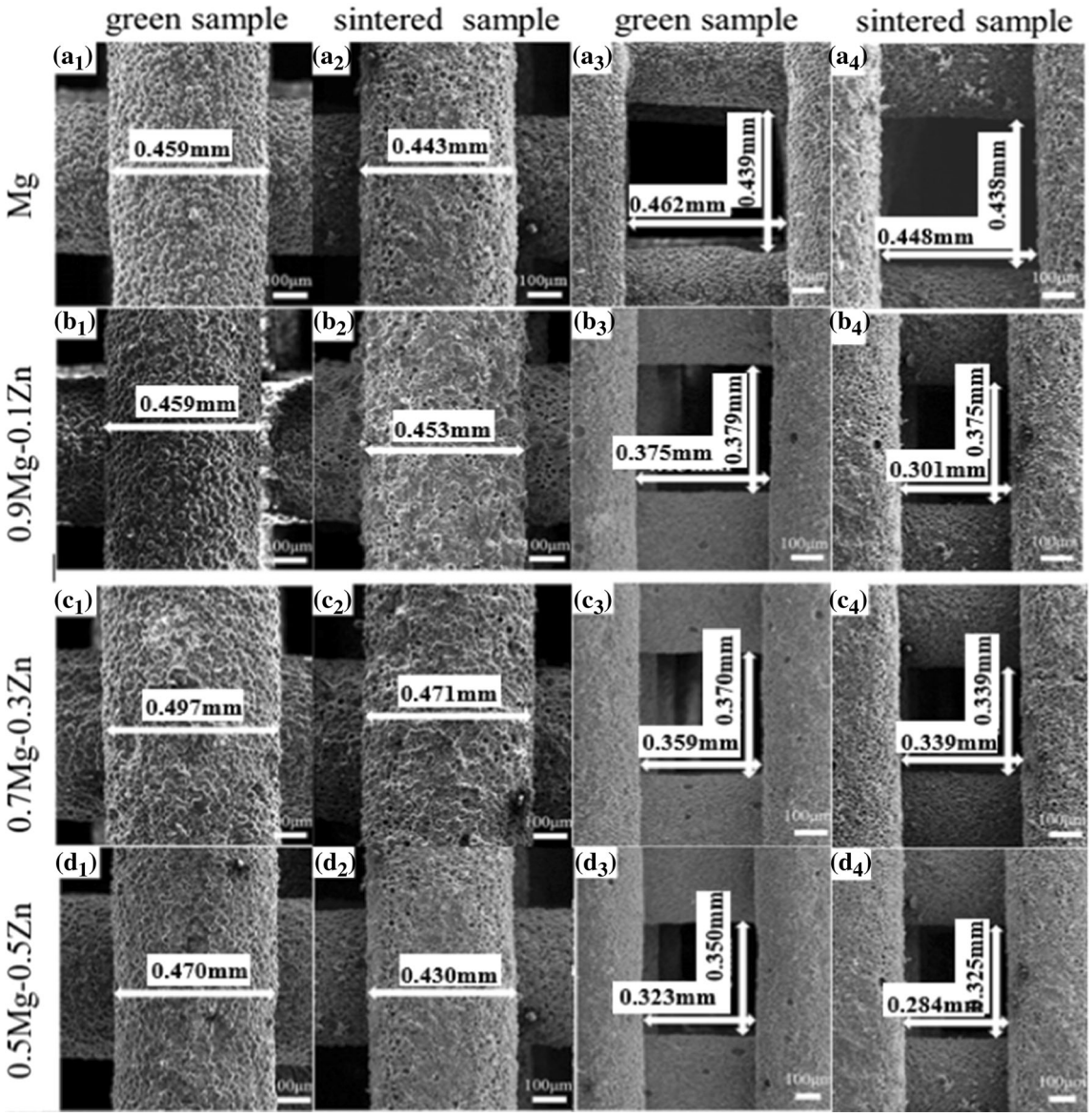

Figure 6 SEM images of porous Mg–*x*Zn scaffolds printed by 3DGP.

addition of Zn powder, and μ_r decreases. At the same shear rate, the lower the viscosity, the easier the slurry extrusion.

Excellent stock with suitable printing parameters is required to print magnesium supports with excellent performance successfully. Table 1 shows the 3DGP printing parameters of porous Mg–*x*Zn scaffolds. The printed surface will be damaged if the printing layer height is too low. If the printing layer height is set too high, the adhesion of the printing line is not good. The printing speed and air pressure should be matched with each other. When the printing wire cannot be squeezed out or ruptured, it can be changed by slowing down the printing speed or increasing the air pressure; when the printing line is bent, it can be altered by increasing the printing speed or reducing the air pressure.

Characteristics of porous Mg–*x*Zn scaffolds

Figure 5 shows the photographs of green (**a**) and sintered (**b**) scaffolds of pure Mg printed by 3DGP. After measurement, the size of the green sample and modeling (24 mm × 24 mm × 5 mm) are basically similar, and the error is within 0.1 mm. The SEM images of porous Mg–*x*Zn scaffolds with different Zn contents are shown in Fig. 6. Before sintering, the

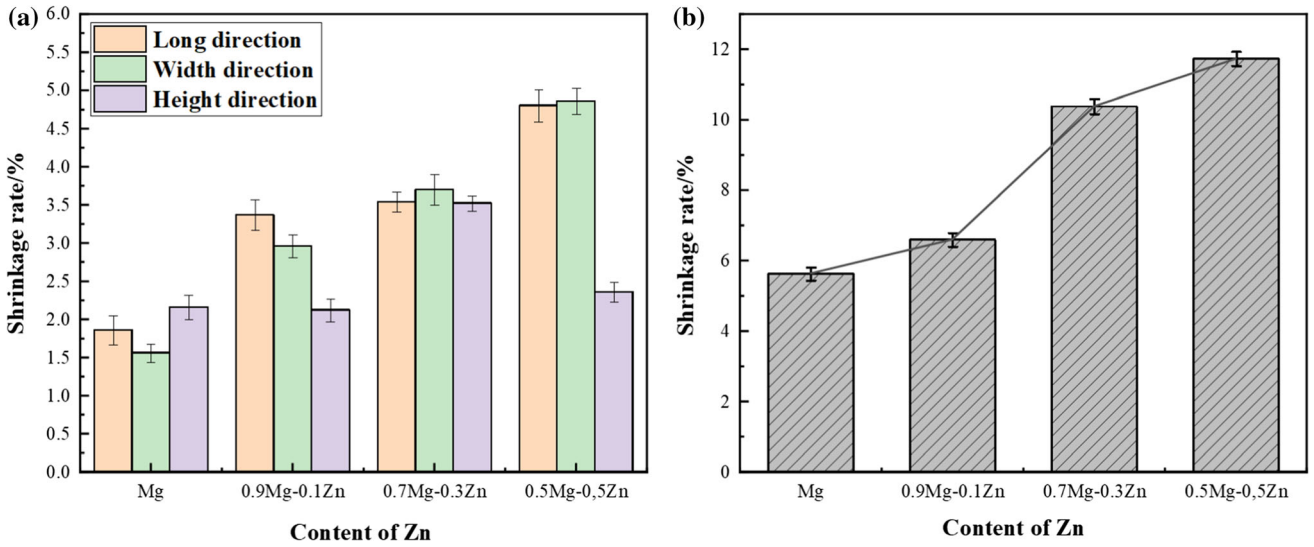

Figure 7 **a** Shrinkage rate of sintered samples with different Zn content, **b** shrinkage rate of samples with different zinc content.

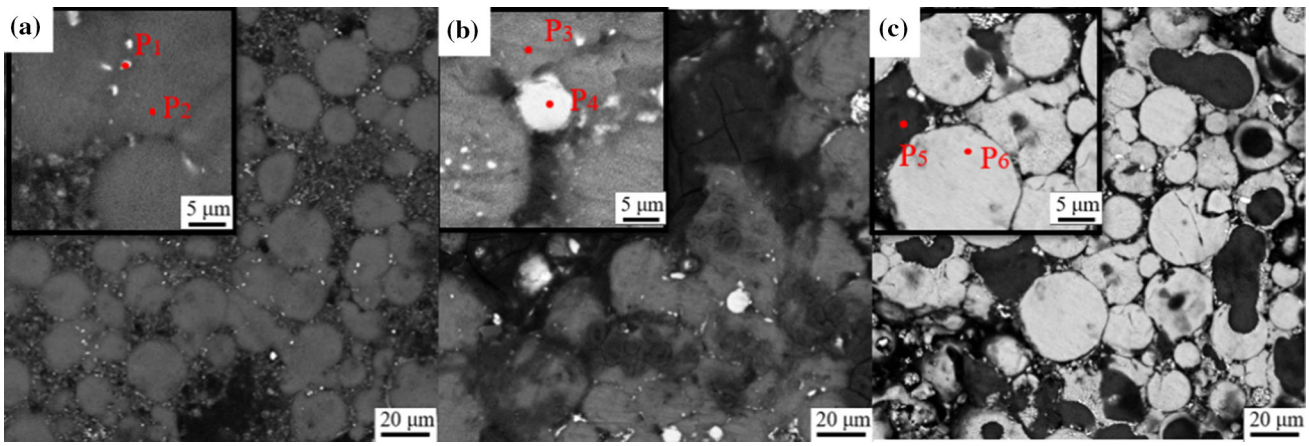

Figure 8 BSD of porous Mg–*x*Zn scaffolds: **a** 0.9Mg–0.1Zn; **b** 0.7Mg–0.3Zn; **c** 0.5Mg–0.5Zn.

Table 2 EDS results of different positions marked in Fig. 8

Positions (atom%)	P_1	P_2	P_3	P_4	P_5	P_6
Mg	41.4	95.7	96.5	68.8	95.4	68.4
Zn	58.6	4.3	3.5	31.2	4.6	31.6

connection between printing wires is good. Mg and Zn powder particles of each scaffold filament were complete and spherical. According to Fig. 7a, the shrinkage in each direction does not exceed 5%, indicating that the 3DGP technique of Mg scaffolds has good dimensional accuracy. In addition, the shrinkage rate increased slightly following the increase in Zn content. Calculating the single-wire shrinkage rates of Mg, 0.9Mg–0.1Zn, 0.7Mg–0.3Zn, and 0.5Mg–0.5Zn are 2.7%, 6.7%, 7.6%, and 8.6%, respectively, shown are in Fig. 7b. Zn is lost in liquid during sintering because the melting point of Zn is low. With the increase in Zn content, the solid phase of the sample decreases, and the shrinkage rate of single wire increases.

Microstructure of porous Mg–*x*Zn scaffolds

As shown in Fig. 8, the microstructures of the three different Mg–Zn scaffolds consists of bright white and dark phases. According to the EDS energy spectrum analysis, the dark phase is the Mg matrix, while the bright white phase is the intermetallic compound phase of Mg–Zn. As the Zn content increases from 10 to 30 wt%, the intermetallic

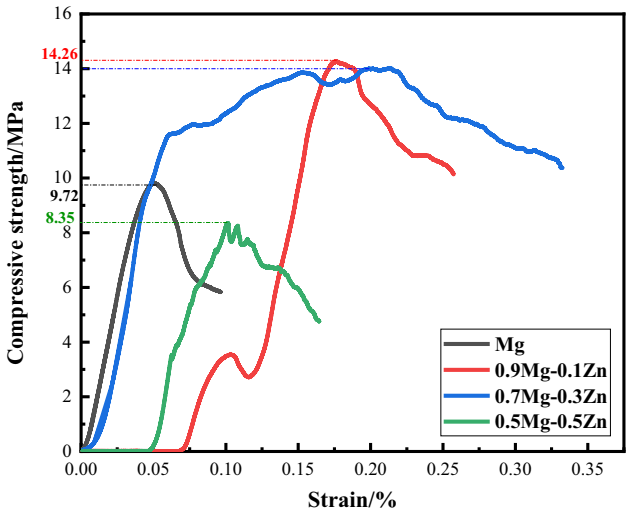

Figure 9 Compressive strength curve of sintered porous Mg–*x*Zn scaffolds by 3DGP.

compound phase gradually changes from fine and diffuse distribution at grain boundaries to an increase in the size of a few grains, still distributed at grain boundaries. The bright white intermetallic compounds are determined to be MgZn and Mg_7Zn_3 based on the EDS compositions of points P1 and P4 in Table 2 and the Mg–Zn binary phase diagram. When the content reaches 50 wt%, more Zn diffuses into the magnesium grains, forming a large intermetallic compound of equiaxed grains, which indicates a coarser overall grain size and a greatly reduced volume fraction of the magnesium matrix. The composition of the P6 point shows that the alloy phase is still Mg_7Zn_3.

Mechanical properties of porous Mg–*x*Zn scaffolds

Figure 9 shows the compressive strength curve of porous sintered Mg–*x*Zn scaffolds printed by 3DGP. The compressive strengths of Mg, 0.9Mg–0.1Zn, 0.7Mg–0.3Zn, and 0.5Mg–0.5Zn porous scaffolds are about 6.29 MPa, 13.03 MPa, 7.69 MPa, and 6.61 MPa, respectively, which meet the cancellous bone requirements (0.1–16 MPa). According to the hardness in Table 3, the Zn content increases and the hardness values increase. This is related to the microstructure formed, as shown in Fig. 8, which indicates that the equiaxed grains in the organization of the 0.5Mg–0.5Zn scaffold are Mg–Zn compounds and that the hardness of the Mg–Zn complex is greater than that of pure magnesium.

The 0.9Mg–0.1Zn sample and the 0.7Mg–0.3Zn sample exhibited higher strength due to diffusion strengthening and second-phase strengthening mechanisms [28, 29]. For the 0.5Mg–0.5Zn sample, a large amount of Mg_7Zn_3 alloy phase precipitates mixed with the magnesium matrix. Many holes are left after the loss of Zn in liquid due to the high sintering temperature, which results in lower strength of 0.5Mg–0.5Zn scaffolds than the other components of scaffolds. Zn powder with a small particle size can be filled into the gaps between Mg powder, which helps improve the density and compressive strength of samples. The porosity of the scaffold with different Zn contents after sintering is listed in Table 3. The porosity decreases with 10% Zn and increases again with the continued addition of Zn. This is because the scaffold undergoes a degreasing process during sintering, vaporizing organic matter and leaving more pores. In contrast, thermal sintering at high temperatures causes Zn to become liquid and fill pores. However, a large amount of Zn content causes a small amount of Zn to evaporate and float on the surface of the scaffold, so adding a small amount of Zn will reduce the porosity. Adding a large amount of zinc increases the porosity again, but the difference in porosity is not large, in the 50–60% range. Since the macroscopic macropores of the scaffold itself are controllable and play a more critical role in bone attachment, the reduction in microscopic porosity of the metal printing wire does not cause a more significant impact. However, it will improve the strength to a certain extent.

Table 3 Porosity and mechanical properties of the samples

Sample	Porosity (%)	Microhardness (MPa)	UCS (MPa)	Modulus (GPa)
Mg	59.03 ± 0.35	52.77 ± 1.1	9.72 ± 0.03	0.23 ± 0.02
0.9Mg–0.1Zn	52.31 ± 0.34	64.44 ± 1.2	14.26 ± 0.05	0.24 ± 0.02
0.7Mg–0.3Zn	59.32 ± 0.42	74.82 ± 1.4	14.00 ± 0.02	0.29 ± 0.03
0.5Mg–0.5Zn	56.96 ± 0.53	99.18 ± 1.5	8.35 ± 0.05	0.17 ± 0.01

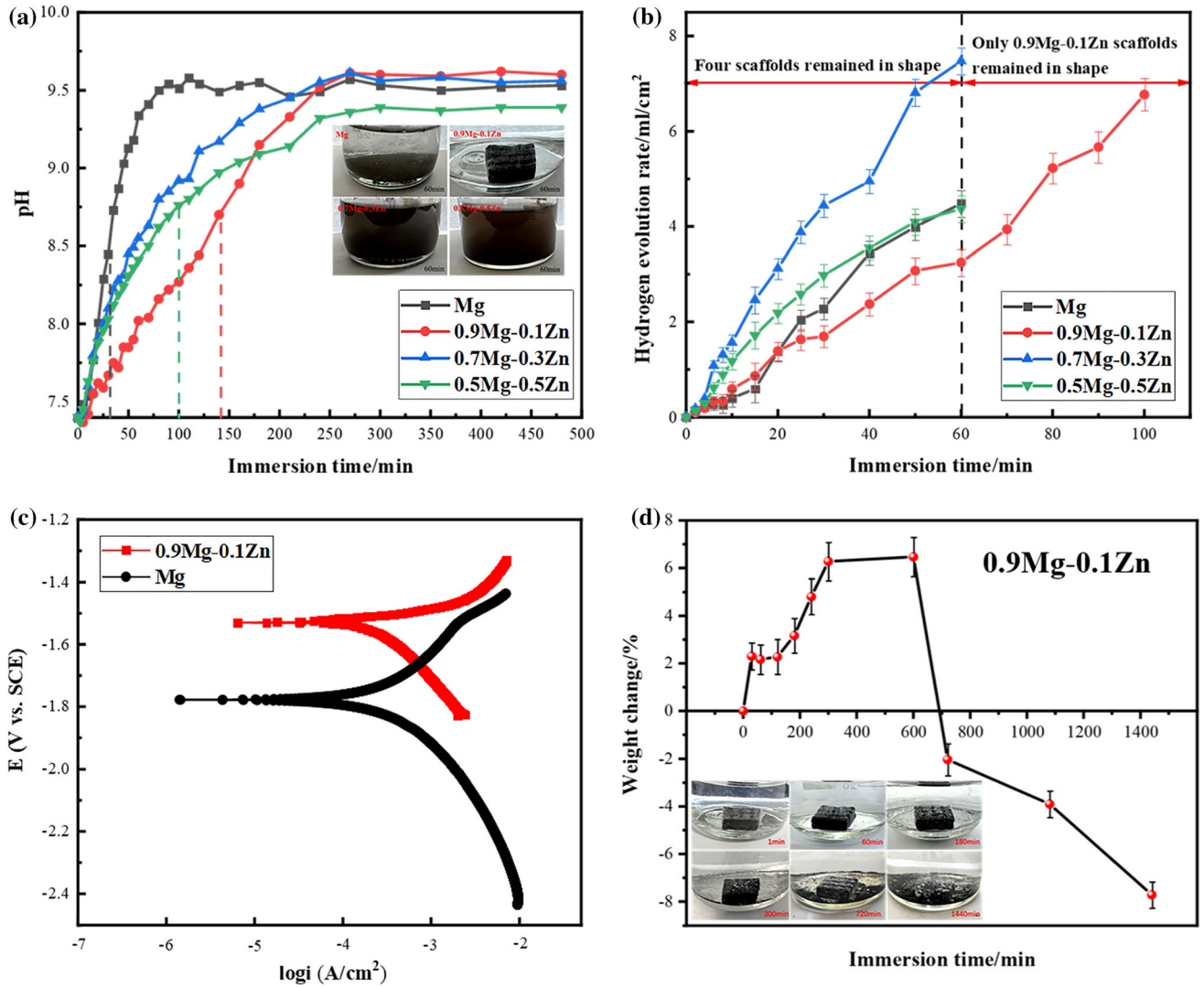

Figure 10 **a** The pH of degradation solution and **b** hydrogen evolution rate for porous Mg–*x*Zn scaffolds; **c** potentiodynamic polarization curves and **d** the weight change percentage of 0.9Mg–0.1Zn porous scaffolds.

In vitro degradation of porous Mg–*x*Zn scaffolds

Figure 10a and b shows the relation between the pH value and hydrogen evolution rate of degradation solution and degradation time for porous Mg, 0.9Mg–0.1Zn, 0.7Mg–0.3Zn, and 0.5Mg–0.5Zn scaffolds, respectively. The pH value of the degradation solution increased with the progress of the reaction and tended to be stable after the scaffolds were utterly degraded. During the reaction, a large amount of hydrogen was produced on the surface of the scaffolds, and the solution gradually became turbid. The Mg scaffold began to collapse at 40 min and lost its strength. After 4 h, the reaction was complete, and the pH was stable at about 9.53. The pH of 0.7Mg–0.3Zn changes rapidly and its hydrogen precipitation rate was the fastest. However, the 0.5Mg–0.5Zn scaffold showed an intense degradation. It reacted violently after immersing in the SBF solution and generated many bubbles. After 20 min, the scaffold was almost degraded to powder. The 0.9Mg–0.1Zn scaffold had the best corrosion resistance with the slowest pH change rate and hydrogen precipitation rate. The scaffolds collapsed only after 24 h of immersion and degraded completely to powder only after 48 h. Therefore, the weight change of the 0.9Mg–0.1Zn stent was tested and recorded (Fig. 10d), and it was found that the stent had been in a weight gain state for the first 10 h, which originated

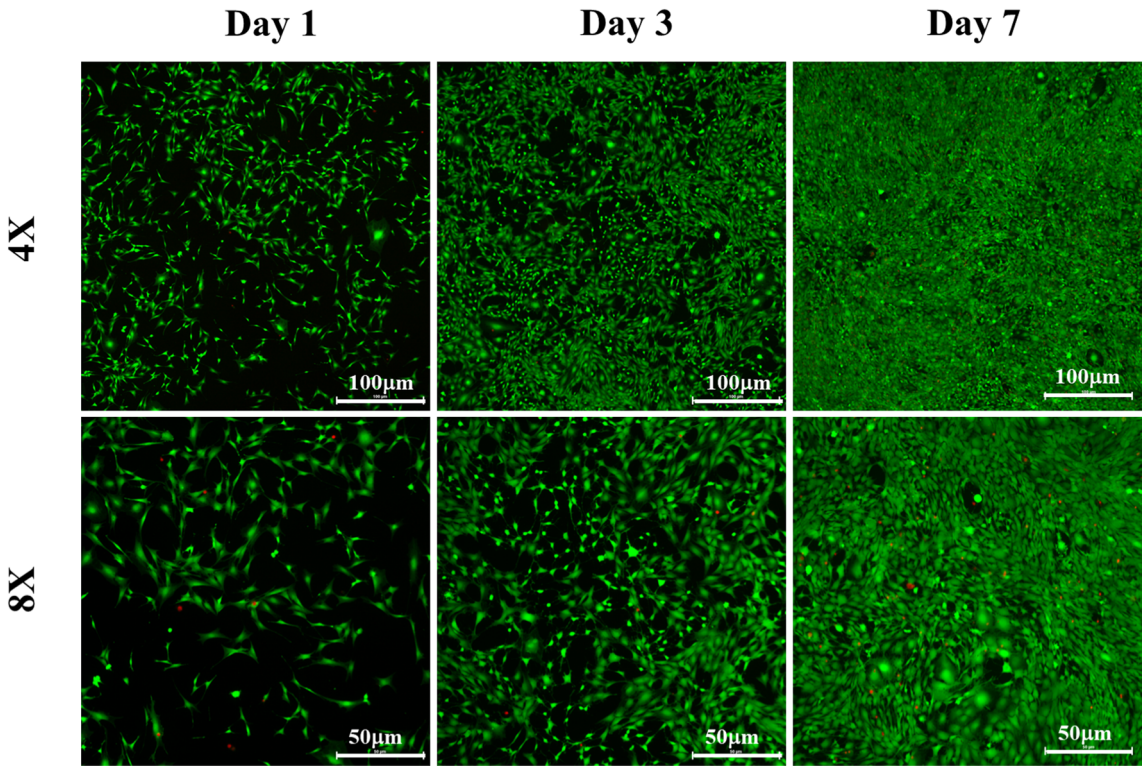

Figure 11 Live/dead staining assay of MC3T3-E1 cells with 0.9Mg–0.1Zn scaffold material extract for 1, 3 and7days.

from the white corrosion products attached to the surface of the scaffold. And there was a small amount of debris around the stent after 5 h, and the scaffold was in a weight loss state after 12 h.

Furthermore, this study tested the best corrosion-resistant 0.9Mg–0.1Zn alloy electrochemically and compared it with pure Mg. As shown in Fig. 10c, the E_{corr} and I_{corr} of 0.9Mg–0.1Zn alloy and pure Mg were − 1.52 V, − 1.77 V, and 239.17 μA, 423.86 μA, respectively. The alloy's corrosion potential and corrosion current with 10% Zn addition were significantly less than those of pure Mg [30, 31].

The main reason for the large differences in the degradation rates of the four scaffolds is the different states of the intermetallic phases in their microstructures. 0.9Mg–0.1Zn scaffold has a fine and diffuse distribution of MgZn alloy phase, so its strengthening mechanism acts more than galvanic corrosion and shows better corrosion resistance than pure Mg. However, the volume fraction of Mg–Zn intermetallic compounds in the 0.7Mg–0.3Zn and 0.5Mg–0.5Zn scaffolds increased considerably, and equiaxed grains of compounds with larger diameters appeared. In particular, the 0.5Mg–0.5Zn scaffold formed a large area of Mg_7Zn_3 equiaxed crystalline compound and fine and distributed MgZn phase at the grain boundaries due to the diffusion of Zn into the Mg powder, which caused severe galvanic corrosion [32]. Because of the large potential difference between the Mg_7Zn_3 phase, MgZn phase and Mg matrix, the Mg matrix acts as the anode and the alloy phase acts as the cathode when the two exist simultaneously. Therefore, when the body liquid is immersed in the material pores, it triggers galvanic coupling corrosion and accelerates degradation [33, 34].

The addition of small amounts of Zn, such as 1%, 4%, and 6%, has been shown to be effective in slowing down the degradation and improving the mechanical properties. Combined with the addition of 10%, 30% and 50% Zn in this paper, a comprehensive analysis shows that the addition of $\leq$ 10% Zn is more effective in improving the overall performance of magnesium alloys. The effect of adding either a large or small percentage of Zn elements on the magnesium alloy support depends on the size, morphology, and distribution state of the intermetallic compound. The galvanic coupling corrosion caused by the alloy phase is the key to accelerating the degradation of Mg–Zn alloy; if this effect can be

eliminated, it can significantly improve its corrosion resistance.

Due to the large specific surface area, the degradation of porous magnesium scaffolds is inevitably faster than that of dense magnesium scaffolds. The results show that the degradation of porous Mg scaffolds can be slowed down by adding proper amount of Zn ($x \leq 10\%$Zn). In order to better retard the degradation of magnesium scaffolds and enable the effective growth of trabecular bone around the scaffolds, the next step is to further study the surface modification of Mg–Zn alloy scaffolds.

Biological performance of porous Mg–Zn scaffolds

The SM image after cell staining is shown in Fig. 11. The green spots are live cells, and the red spots are dead cells. Cell activity results showed that the number of living cells on the 7th day was significantly higher than that on the 3rd day. The number of green living cells on the 3rd day was significantly higher than that on the 1st day, indicating that the scaffold material promoted the proliferation of MC3T3-E1 cells. TheMg^{+} released by degradation improved the osteogenic ability. Therefore, 0.9Mg–0.1Zn scaffolds have good cytocompatibility.

Conclusions

In this paper, we not only successfully printed porous Mg–*x*Zn scaffolds with different Zn content by the 3DGP method, but also tried to study the effect of a larger percentage of Zn content (10, 30, 50 wt%) on Mg–Zn alloy scaffolds. Furthermore, combined with the results of previous studies on the small percentage of Zn content, we comprehensively evaluated the role of elemental Zn on the mechanical and degradation properties of magnesium alloys. For Mg–*x*Zn printing slurry, the low viscosity of the slurry is not easy to form, and high viscosity will block the needle. The results show that when the solid content is about 60%, it is suitable for printing because of its good formability and uniformity. The compressive strengths of pure Mg, 0.9Mg–0.1Zn, 0.7Mg–0.3Zn, and 0.5Mg–0.5Zn porous scaffolds are 6.29 MPa, 13.03 MPa, 7.69 MPa, and 6.61 MPa, respectively, which meet the cancellous bone requirements (0.1–16 MPa). In vitro simulated body fluid degradation tests showed that an appropriate amount of Zn can slow down the degradation of Mg scaffolds. However, excessive addition will reduce the corrosion resistance of scaffolds. On the whole, galvanic corrosion caused by the alloy phase in the microstructure is the key to accelerating the degradation of Mg–*x*Zn alloys. If this effect can be eliminated, its corrosion resistance will significantly improve.

Acknowledgements

This work was supported by Science and Technology Projects of Guangdong Province, P.R. China (Grant No. 2016B090914001) and Jihua Laboratory Project "Additive Manufacturing for Difficulty-to-Machine Materials" (Grant No.X190061UZ190).

Author contributions

TL involved in investigation, conceptualization, methodology, writing—original draft preparation, writing—reviewing, and editing. JD involved in investigation, formal analysis, writing—original draft, and data curation. XW involved in writing—reviewing, and editing. XD involved in writing—reviewing, and editing. HS involved in resources, funding acquisition, and supervision.

Declarations

Conflict of interest The authors declare that they have no known competing financial interests or personal relationships that could have appeared to influence the work reported in this paper.

References

[1] Hou Z, Xiang M, Chen N, Cai X, Zhang B, Luo R et al (2021) The biological responses and mechanisms of endothelial cells to magnesium alloy. Regen Biomater 8(3):13. https://doi.org/10.1093/rb/rbab017

[2] Yang H, Xia K, Wang T, Niu J, Song Y, Xiong Z et al (2016) Growth, in vitro biodegradation and cytocompatibility properties of nano-hydroxyapatite coatings on biodegradable magnesium alloys. J Alloys Compd 672:366–373. https://doi.org/10.1016/j.jallcom.2016.02.156

[3] Li N, Chen Y, Deng B, Yue J, Qu W, Yang H et al (2019) Low temperature UV assisted sol–gel preparation of ZrO_2 pore-sealing films on micro-arc oxidized magnesium alloy AZ91D and their electrochemical corrosion behaviors. J Alloys Compd 792:1036–1044. https://doi.org/10.1016/j.jallcom.2019.04.124

[4] Wang T, Yang G, Zhou W, Hu J, Jia W, Lu W (2019) One-pot hydrothermal synthesis, in vitro biodegradation and biocompatibility of Sr-doped nanorod/nanowire hydroxyapatite coatings on ZK60 magnesium alloy. J Alloys Compd 799:71–82. https://doi.org/10.1016/j.jallcom.2019.05.338

[5] Bütev Öcal E, Esen Z, Aydınol K, Dericioğlu AF (2020) Comparison of the short and long-term degradation behaviors of as-cast pure Mg, AZ91 and WE43 alloys. Mater Chem Phys 241:122350. https://doi.org/10.1016/j.matchemphys.2019.122350

[6] Chaudry UM, Farooq A, Kb T, Malik A, Kamran M, Kim J-G et al (2022) Corrosion behavior of AZ31 magnesium alloy with calcium addition. Corros Sci 199:110205. https://doi.org/10.1016/j.corsci.2022.110205

[7] Jiang P, Blawert C, Zheludkevich ML (2020) The corrosion performance and mechanical properties of Mg–Zn based alloys—a review. Corros Mater Degrad 1(1):92–158. https://doi.org/10.3390/cmd1010007

[8] Zhang HD, Chen AY, Gan B, Jiang H, Gu LJ (2022) Corrosion protection investigations of carbon dots and polydopamine composite coating on magnesium alloy. J Magnes Alloys 10(5):1358–1367. https://doi.org/10.1016/j.jma.2020.11.021

[9] Zhang Q, Chen Z, Li Q, Chen X, Zhao J, Bao J (2021) Deformation behavior characterized by reticular shear bands and long chain twins in Mg–Gd-Nd(–Zn)–Zr alloys. J Mater Res Technol 15:5326–5342. https://doi.org/10.1016/j.jmrt.2021.11.020

[10] Mena-Morcillo E, Veleva L (2020) Degradation of AZ31 and AZ91 magnesium alloys in different physiological media: effect of surface layer stability on electrochemical behaviour. J Magnes Alloys 8(3):667–675. https://doi.org/10.1016/j.jma.2020.02.014

[11] Liu A-h, Xu J-l (2018) Preparation and corrosion resistance of superhydrophobic coatings on AZ31 magnesium alloy. Trans Nonferrous Met Soc China 28(11):2287–2293. https://doi.org/10.1016/s1003-6326(18)64873-3

[12] Zhang X, Wu Y, Xue Y, Wang Z, Yang L (2012) Biocorrosion behavior and cytotoxicity of a Mg–Gd–Zn–Zr alloy with long period stacking ordered structure. Mater Lett 86:42–45. https://doi.org/10.1016/j.matlet.2012.07.030

[13] Feng Y, Zhu S, Wang L, Chang L, Hou Y, Guan S (2018) Fabrication and characterization of biodegradable Mg–Zn–Y–Nd–Ag alloy: microstructure, mechanical properties, corrosion behavior and antibacterial activities. Bioact Mater 3(3):225–235. https://doi.org/10.1016/j.bioactmat.2018.02.002

[14] Dong J, Lin T, Shao H, Wang H, Wang X, Song K et al (2022) Advances in degradation behavior of biomedical magnesium alloys: a review. J Alloys Compd 908:164600. https://doi.org/10.1016/j.jallcom.2022.164600

[15] Song G (2007) Control of biodegradation of biocompatable magnesium alloys. Corros Sci 49(4):1696–1701. https://doi.org/10.1016/j.corsci.2007.01.001

[16] Jarzębska A, Bieda M, Maj Ł, Chulist R, Wojtas D, Strąg M et al (2020) Controlled grain refinement of biodegradable Zn–Mg alloy: the effect of magnesium alloying and multi-pass hydrostatic extrusion preceded by hot extrusion. Metall Mater Trans A 51(12):6784–6796. https://doi.org/10.1007/s11661-020-06032-4

[17] Dong J, Li Y, Lin P, Leeflang MA, van Asperen S, Yu K et al (2020) Solvent-cast 3D printing of magnesium scaffolds. Acta Biomater 114:497–514. https://doi.org/10.1016/j.actbio.2020.08.002

[18] Ren X, Shao H, Lin T, Zheng H (2016) 3D gel-printing-an additive manufacturing method for producing complex shape parts. Mater Des 101:80–87. https://doi.org/10.1016/j.matdes.2016.03.152

[19] Zhang Z, Lin T, Shao H, Peng J, Wang A, Zhang Y et al (2020) Effect of different dopants on porous calcium silicate composite bone scaffolds by 3D gel-printing. Ceram Int 46(1):325–330. https://doi.org/10.1016/j.ceramint.2019.08.266

[20] Zhang Y, Shao H, Lin T, Peng J, Wang A, Zhang Z et al (2019) Effect of Ca/P ratios on porous calcium phosphate salt bioceramic scaffolds for bone engineering by 3D gel-printing method. Ceram Int 45(16):20493–20500. https://doi.org/10.1016/j.ceramint.2019.07.028

[21] Wu CL, Zai W, Man HC (2021) Additive manufacturing of ZK60 magnesium alloy by selective laser melting: parameter optimization, microstructure and biodegradability. Mater Today Commun 26:101922. https://doi.org/10.1016/j.mtcomm.2020.101922

[22] Yang G, Wang C, Wang C, Wang J, Liu D (2022) Effect of Gd element on corrosion rate of SLM formed medical magnesium alloy. Rare Metal Mater Eng 51(6):2167–2174

[23] Gunasekaran J, Sevvel P, Solomon IJ (2021) Metallic materials fabrication by selective laser melting: a review. Mater Today Proc 37:252–256. https://doi.org/10.1016/j.matpr.2020.05.162

[24] Cai S, Lei T, Li N, Feng F (2012) Effects of Zn on microstructure, mechanical properties and corrosion behavior of Mg–Zn alloys. Mater Sci Eng C Mater Biol Appl

32(8):2570–2577. https://doi.org/10.1016/j.msec.2012.07.042

[25] Lin T, Li Q, Song K, Shao H, Yuan J, Deng X (2021) Preparation of TiC reinforced CrMo steel by 3D gel-printing. Powder Metall 64(5):360–369. https://doi.org/10.1080/00325899.2021.1911068

[26] Lin T, Jin L-P, Yuan J-Y, Shao H-P, Yu F-C, Li W-Y et al (2021) Direct ink writing of TiC-316L metal matrix composites with an epoxy resin-absolute ethanol system. Rare Met 40(3):590–599. https://doi.org/10.1007/s12598-020-01611-1

[27] Yin S, Duan W, Liu W, Wu L, Yu J, Zhao Z et al (2020) Influence of specific second phases on corrosion behaviors of Mg–Zn–Gd–Zr alloys. Corros Sci 166:108419. https://doi.org/10.1016/j.corsci.2019.108419

[28] Wang Y, Zhong L, Dou Y, Huang Z (2021) Enhanced age hardening response and precipitation evolution of elastic stress aged Mg–Zn alloys. J Alloys Compd 860:158513. https://doi.org/10.1016/j.jallcom.2020.158513

[29] Alizadeh R, Wang J, Llorca J (2021) Precipitate strengthening of pyramidal slip in Mg–Zn alloys. Mater Sci Eng A 804:140697. https://doi.org/10.1016/j.msea.2020.140697

[30] Pan Y, He S, Wang D, Huang D, Zheng T, Wang S et al (2015) In vitro degradation and electrochemical corrosion evaluations of microarc oxidized pure Mg, Mg–Ca and Mg–Ca–Zn alloys for biomedical applications. Mater Sci Eng C Mater Biol Appl 47:85–96. https://doi.org/10.1016/j.msec.2014.11.048

[31] Dong H, Lin F, Boccaccini AR, Virtanen S (2021) Corrosion behavior of biodegradable metals in two different simulated physiological solutions: comparison of Mg Zn and Fe. Corros Sci 182:109278. https://doi.org/10.1016/j.corsci.2021.109278

[32] Thekkepat K, Han H-S, Choi J-W, Lee S-C, Yoon ES, Li G et al (2022) Computational design of Mg alloys with minimal galvanic corrosion. J Magnes Alloys 10(7):1972–1980. https://doi.org/10.1016/j.jma.2021.06.019

[33] Tong F, Chen X, Wang Q, Wei S, Gao W (2021) Hypoeutectic Mg–Zn binary alloys as anode materials for magnesium–air batteries. J Alloys Compd 857:157579. https://doi.org/10.1016/j.jallcom.2020.157579

[34] Feng B, Liu G, Yang P, Huang S, Qi D, Chen P et al (2022) Different role of second phase in the micro-galvanic corrosion of WE43 Mg alloy in NaCl and Na_2SO_4 solution. J Magnes Alloys 10(6):1598–1608. https://doi.org/10.1016/j.jma.2020.12.013